

Hybrid RF/Optical Communications via 34-meter DSN Antennas

Victor A. Vilnrotter*

There is considerable interest in determining whether suitably modified versions of existing 34-m antennas at NASA's Goldstone Communications Complex, originally designed for X-band (nominally 8 GHz) and Ka-band (32 GHz) operation, could also be used to receive near-infrared optical signals. The robust backup structure of these antennas, together with extremely large collecting apertures and millidegree pointing capabilities, suggest that dual RF/optical communications may indeed be possible, at optical data rates approaching 1 gigabit per second (GBPS) from typical Mars distances. Several design concepts have emerged as possible candidates, requiring modifications ranging from polishing and coating of the existing aluminum panels of the main reflector, to significant redesign involving replacement of the panels with optical reflectors. Optical receiver parameters such as collecting area, field of view (FOV), and immunity to reflected sunlight differ markedly for each design concept, hence will likely lead to different levels of performance in terms of data throughput at a given error probability, and in terms of the ability to point close to the Sun. The communications performance of two candidate design concepts operating under realistic daytime conditions is evaluated, with particular emphasis on spatial and temporal acquisition algorithms and receiver optimization to achieve the best possible communication performance at high data rates.

I. Introduction

Optical communication requires the establishment of a cooperative link between the transmitter and the receiver before any data transfer can occur. In a typical scenario, the transmitter may initiate data transfer by pointing a narrow laser beam in the direction of the receiver, with point-ahead if necessary to ensure that the center of the beam reaches the receiver. Next, the receiver points its optical axis in the nominal direction of the spacecraft transmitter, refining the pointing to center the focused laser signal over the receiver's high-speed communications detector array: this operation is called spatial acquisition. Following spatial acquisition, the receiver continues to monitor the center of the focused spot and corrects for slow drifts in mechanical pointing, then proceeds to establish temporal acquisition to determine the boundaries of the data symbols and codeword frames before detecting the data. As with spatial acquisition, temporal acquisition is followed by tracking to correct for

* Communication Architectures and Research Section.

The research described in this publication was carried out by the Jet Propulsion Laboratory, California Institute of Technology, under a contract with the National Aeronautics and Space Administration. © 2010 California Institute of Technology. Government sponsorship acknowledged.

slow drifts in the symbol boundaries due to transmitter clock instabilities or other sources of error.

These two operations can be carried out sequentially as described, or iteratively whereby partial information about the symbol boundaries is transferred from the temporal acquisition system to the spatial acquisition system, and used to reduce background interference via temporal windowing thus aiding spatial acquisition, which in turn leads to more precise centering of the signal energy. Note that with any implementation, some degree of spatial acquisition must occur first in order to receive signal energy, hence it can be argued that signal acquisition is inherently a sequential operation, even if temporal acquisition and aiding begins before the spatial acquisition process is completed. Here we consider only the sequential approach, treating spatial and temporal acquisition as separate operations within the receiver, in order to emphasize the key features of each technique.

We begin by describing the approaches considered for implementing a hybrid RF/optical receiver for the Deep Space Network (DSN) in Section II. The mathematical model required to derive the structure and performance of these optical receivers is developed in Section III. Spatial acquisition is treated in Section IV, and temporal acquisition in Section V. Finally, uncoded data detection performance of the optical receiver after successful spatial and temporal acquisition is optimized and evaluated in Section VI, and coding options to further improve performance are discussed.

II. Hybrid RF/Optical Antenna Receiver Options

The hybrid RF/optical receiver concepts considered here can be grouped into two general categories: optical receivers with very large collecting apertures making use of the existing RF panels, polished to optical smoothness but operating with large fields of view (FOVs) due to surface imperfections; and smaller-aperture optical receivers relying on high-quality glass mirrors that replace a fraction of the aluminum panels of the antenna to achieve much smaller optical FOVs, while still maintaining adequate RF performance.

From the viewpoint of optical communications, the most important performance metrics include spatial acquisition, temporal acquisition, and symbol detection, all of which depend on the amount of signal and background photons collected by the receiver, and their distribution in space and time. In this context, the specific details of the optical-mechanical design are not very significant, as long as each design generates the same key parameters, namely point-spread function (PSF), and average signal photons and average background photons collected by the receiver in a given time. Although the choice of optical-mechanical design may impact cost and complexity, and the required reconfiguration of the existing 34-m antennas may vary markedly with different designs, performance characteristics can be determined from the ability to collect signal photons and reject background photons by concentrating the signal energy into a small PSF in the detector plane.

The design of optical photon-counting receivers to operate at a given data rate and symbol error probability is often more complicated than RF receiver design, because in the optical domain communications performance is determined by Poisson statistics, where a single

parameter such as signal-to-noise ratio (SNR) cannot generally be used to predict performance. In RF communications, where the signal is observed in the presence of additive white Gaussian noise, SNR is indeed the correct performance metric. The following example illustrates this concept by comparing a small optical receiver aperture with perfect optics that achieves diffraction-limited performance, thus virtually eliminating background, with a much larger but less-precise optical collecting aperture operating with a larger FOV, therefore collecting significantly more background but also collecting more signal photons.

Assume the laser link employs pulse-position modulation (PPM) with $M \gg 1$ slot per symbol. If the smaller-aperture receiver collects an average of $K_s = 4$ photons per laser pulse, and limits background light to insignificant levels via spatial and optical filtering, then the probability of symbol error, PSE, is roughly the probability of an erasure for a Poisson process with rate K_s , namely $PSE = \exp(-K_s) \approx 0.02$. However, an aperture with 10 times the area would collect 40 signal photons on the average. Even if the FOV of this larger receiver were much greater, so that it collected many more interfering background photons per PPM slot, K_b , the performance of this receiver could be better than that of the diffraction-limited receiver because of the greater amount of signal photons it collects. To illustrate this point, it can be seen from Figure 8.5c in [1] that with $K_s = 40$ and $K_b = 10$, the symbol error probability is $PSE \leq 10^{-6}$ as long as $M < 100$. Unlike in optical imaging, where diffraction-limited optics are essential for producing a good image, in optical communications collecting signal photons is often more important than diffraction-limited performance, even at the cost of admitting more background photons into the receiver.

Two hybrid RF/optical receiver options will be considered:

- (1) A 26-m design that utilizes the inner 26 m of solid aluminum panels on a 34-m antenna, polished to reflect near-infrared signals but generating somewhat large (several centimeters diameter) spots at the Cassegrain focus corresponding to FOVs of hundreds of microradians.
- (2) A 10-m design that uses high-quality glass optics and produces much smaller focused spots typically limited by turbulence to approximately 50 μrad .

III. Mathematical Model of Focal-Plane Array Processing

Performance of both optical receiver options depends on the method of detection employed at the respective focal planes, and on the signal-processing algorithms used to implement the required functions. Here we assume that detection takes place via a photon-counting detector array of sufficient dimensions to capture the required fraction of signal photons from the turbulence-degraded average PSF. It is assumed that the dimensions of each detector element, or subarray of detector elements connected together to function as a single detector, are sufficiently large to encompass a great many spatial modes at any given time. For example, a 26-m-diameter optical receiver with 100-m effective focal length, observing turbulence-degraded optical fields with a coherence-length of $r_0 = 3$ cm, would generate a PSF at 1550 nm of approximately $100 \times 1.55 \times 10^{-6} / 3 \times 10^{-2} \approx 0.5 \times 10^{-2}$ m, or approximately 0.5 cm in diameter. This PSF contains roughly $(26/.03)^2 = 7.5 \times 10^5$ spatial modes in a 5-mm-square area, or 300 modes over a 0.1-mm-square detector element or

subarray. So many modes per detector element suggests that a form of “aperture-averaging” can be invoked for the detector elements or subarrays, and hence the received intensity can be treated as a constant rather than a randomly fluctuating intensity. We shall therefore assume this simplified model in the following analysis, and ignore the small intensity fluctuations on the timescale of milliseconds due to turbulence over the detector elements.

To facilitate analysis, the detector plane is modeled as a large array of small detector elements (or subarrays), essentially covering the extent of the PSF plus any uncertainty in its center coordinates before spatial acquisition (centering) has taken place. This does not imply that the actual physical detector-array has to be very large, but merely suggests a reasonable size for implementation. The key elements of the detector-plane model are shown in Figure 1, assuming that enough spatial modes are impinging on each detector element to justify the constant PSF intensity assumption.

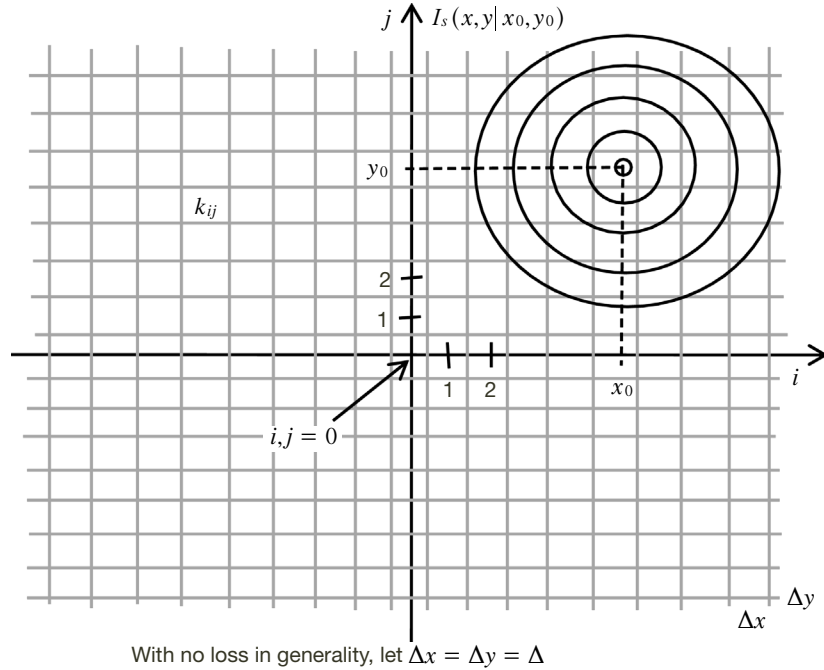


Figure 1. Detector-plane model of photon-counting array and PSF with pointing offsets.

Initially, we assume that background radiation is negligibly small, as would be the case at night through a narrowband optical filter. We therefore set the constant background intensity to zero: $I_b = 0$.

The PSF is assumed to be a two-dimensional Gaussian distribution with center at (x_0, y_0) and intensity

$$I_s(x, y | x_0, y_0) = I_s (2\pi\sigma_s^2)^{-1} \exp\{ -[(x - x_0)^2 + (y - y_0)^2] / 2\sigma_s^2 \} \quad \text{watts / cm}^2 \quad (1)$$

The detector elements are taken to be small squares in this model, with power P_{ij} over the ij th detector element equal to the integral of the intensity distribution over its active area, taken to be

$$P_s(i, j | x_0, y_0) = \int_{(i-1/2)\Delta}^{(i+1/2)\Delta} dx \int_{(j-1/2)\Delta}^{(j+1/2)\Delta} dy I_s(x, y | x_0, y_0) \cong \Delta^2 I_s(i\Delta, j\Delta | x_0, y_0) \text{ watts} \quad (2)$$

Integrating power over time yields energy, or average “count-intensity” λ_s if the received laser energy is measured in terms of photons:

$$\lambda_s(i, j | x_0, y_0) = \int_0^T P_s(i, j | x_0, y_0) dt \cong T\Delta^2 I_s(i\Delta, j\Delta | x_0, y_0) \quad (3)$$

With this model, the photon count from the ij th detector element over a time interval of T seconds is a Poisson-distributed random variable with count probability

$$p(k_{ij} | x_0, y_0) = [\lambda_s(i, j | x_0, y_0)]^{k_{ij}} \exp[-\lambda_s(i, j | x_0, y_0)] / k_{ij}! \quad (4)$$

where we have assumed for now that background photons are negligibly small. Recognizing that counts from different detector elements are independent, and defining the array of counts from the entire array as $\mathbf{k} = [k_{ij}]$, the joint density of the array of counts becomes

$$p(\mathbf{k} | x_0, y_0) = \prod_{i,j} [\lambda_s(i, j)]^{k_{ij}} \exp[-\lambda_s(i, j)] / k_{ij}! \quad (5)$$

where the center of the PSF has been absorbed into the count-intensity function to simplify notation. This is the starting point for deriving the maximum-likelihood (ML) estimators for spatial and temporal acquisition, as well as for ML detection of PPM symbols.

IV. Spatial Acquisition of PSF with a Pointing Offset

Spatial acquisition is the process of estimating the initial offset of the signal PSF and applying this estimate to center the PSF over the detector array. The centering operation should be accurate enough to bring it within range of the spatial tracking algorithm, enabling real-time tracking of the PSF in a closed-loop configuration. Spatial tracking algorithms generate error signals in x and y defined over the focal plane as the PSF drifts off-center, which are then converted to elevation and cross-elevation errors and applied to the antenna pointing assembly or to a small tip-tilt mirror to re-center the PSF over the detector array.

The derivation of the ML estimator of the PSF offset coordinates begins with the log-likelihood function, defined as

$$\begin{aligned} \ln p(\mathbf{k} | x_0, y_0) &= \ln \left\{ \prod_{i,j} [\lambda_s(i, j)]^{k_{ij}} \exp[-\lambda_s(i, j)] / k_{ij}! \right\} \\ &= \sum_{i,j} k_{ij} \ln[\lambda_s(i, j)] - \sum_{i,j} \lambda_s(i, j) - \sum_{i,j} \ln(k_{ij}!) \end{aligned} \quad (6)$$

where the last term is simply a constant that contains no information about the desired parameters and hence can be ignored. Note that the likelihood function is the probability density of the count-array, conditioned on the PSF offsets (x_0, y_0) . It is useful to define the total number of signal photons passing through the aperture in time T as

$$\sum_{i,j} \lambda_s(i,j) = \int_0^T dt \sum_i \sum_j \int_{(i-1/2)\Delta}^{(i+1/2)\Delta} dx \int_{(j-1/2)\Delta}^{(j+1/2)\Delta} dy I_s(x,y) = \int_0^T dt \iint_{\text{detector plane}} I_s(x,y|x_0,y_0) dx dy = \Lambda_s \quad (7)$$

A. Large (Mathematically Infinite) Detector Array

Recognizing that for a suitably large array (which contains essentially all of the offset PSF), this quantity is also a constant independent of the offsets, we obtain the simplified form:

$$\ln p(\mathbf{k}|x_0,y_0) = \sum_{i,j} k_{ij} \ln[\lambda_s(i,j)] - \Lambda_s - \sum_{i,j} \ln(k_{ij}!) \quad (8a)$$

$$\ln p'(\mathbf{k}|x_0,y_0) = \sum_{i,j} k_{ij} \ln[\lambda_s(i,j)] \quad (8b)$$

where “prime” indicates that this is no longer the log of a valid probability density, but a simplified function that nevertheless contains all the information needed to determine the offsets in an optimum manner, based on the observed photon-count array.

Proceeding as in [1], the log-likelihood function is maximized by differentiating with respect to the parameters of interest, setting equal to zero, and solving

$$\begin{aligned} \frac{\partial}{\partial x_0} \ln p'(\mathbf{k}|x_0,y_0) &= - \sum_{i,j} k_{ij} \frac{\partial}{\partial x_0} [(i\Delta - x_0)^2 + (j\Delta - y_0)^2] / 2\sigma_s^2 = \sum_{i,j} k_{ij} (i\Delta - x_0) / \sigma_s^2 = 0 \\ \Delta \sum_{i,j} k_{ij} i &= x_0 \sum_{i,j} k_{ij}; \quad \hat{x}_0 = \Delta \sum_i i \sum_j k_{ij} / \sum_i \sum_j k_{ij} \quad \text{and similarly} \quad \hat{y}_0 = \Delta \sum_j j \sum_i k_{ij} / \sum_i \sum_j k_{ij} \end{aligned}$$

Letting $k_i \equiv \sum_j k_{ij}$, the results are

$$\hat{x}_0 = \Delta \sum_i i k_i / \sum_i k_i \quad \text{and} \quad \hat{y}_0 = \Delta \sum_j j k_j / \sum_j k_j$$

The ML estimates of the offsets, (\hat{x}_0, \hat{y}_0) , are seen to be the centroids of the observed count-vectors obtained by summing the counts in the orthogonal direction. A graphical interpretation of the centroid algorithm is shown in Figure 2, providing a pictorial representation of the summing operation in the orthogonal direction for each offset coordinate.

Note that k_i is obtained by summing the counts along the index j (y-direction) for each index i (x-direction), then using these summed counts to estimate the x-coordinate of the offset via the centroid algorithm, which is the ML estimator of the x-coordinate when the background photons are negligible and the detector array is large enough to contain all of the offset PSF. A similar argument holds for estimating the y-coordinate of the PSF offset.

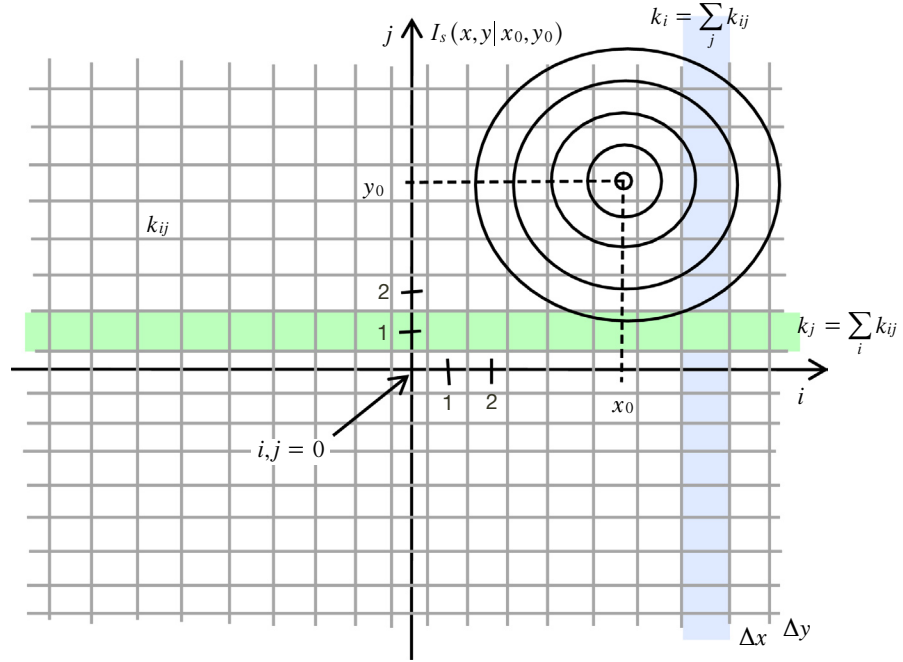


Figure 2. Graphical interpretation of count-vector sum and centroid estimation algorithm.

B. Cramér-Rao Lower Bound on Estimation Variance

For the ideal case of a large detector array observing the signal in the absence of background photons, the Cramér-Rao lower bound on estimation variance is readily derived. According to the Cramér-Rao bound, the variance of any unbiased estimator must exceed the inverse of the expected value of the second derivative of the log-likelihood function with respect to the parameter of interest. In other words, the following inequalities must be satisfied by the estimate of each offset coordinate:

$$\text{var}(\hat{x}_0 - x_0) \geq \left\{ E \left[\frac{\partial^2 \ln p(\mathbf{r} | x_0, y_0)}{\partial x_0^2} \right] \right\}^{-1} \quad \text{var}(\hat{y}_0 - y_0) \geq \left\{ E \left[\frac{\partial^2 \ln p(\mathbf{r} | x_0, y_0)}{\partial y_0^2} \right] \right\}^{-1}$$

The Cramér-Rao bound is computed by first expressing the log-likelihood function explicitly in terms of the parameters of interest:

$$\begin{aligned} \ln p(\mathbf{k} | x_0, y_0) &= \ln \left\{ \prod_{i,j} [\lambda_s(i,j)]^{k_{ij}} \exp[-\lambda_s(i,j)] / k_{ij}! \right\} \\ &= \sum_{i,j} k_{ij} \ln[\lambda_s(i,j)] - \sum_{i,j} \lambda_s(i,j) - \ln(k_{ij}!) \end{aligned}$$

which yields

$$\ln p'(\mathbf{k} | x_0, y_0) = \sum_{i,j} k_{ij} \ln[\lambda_s(i,j)] = - \sum_{i,j} k_{ij} [(i\Delta - x_0)^2 + (j\Delta - y_0)^2] / 2\sigma_s^2 \quad (9)$$

Consider the estimation of the x-coordinate first. Differentiating the log-likelihood function twice with respect to the x-offset yields

$$\begin{aligned}\frac{\partial}{\partial x_0} \ln p'(\mathbf{k} | x_0, y_0) &= -\sum_{i,j} k_{ij} \frac{\partial}{\partial x_0} [(i\Delta - x_0)^2 + (j\Delta - y_0)^2] / 2\sigma_s^2 = \sum_{i,j} k_{ij} (i\Delta - x_0) / \sigma_s^2 \\ \frac{\partial^2}{\partial x_0^2} \ln p'(\mathbf{k} | x_0, y_0) &= -\sum_i \sum_j k_{ij} / \sigma_s^2\end{aligned}$$

Taking the expected value of the counts and inverting yields the Cramér-Rao bound for the variance of the x-coordinate estimate:

$$\text{var}(\hat{x}_0 - x_0) \geq \left\{ -E \left[-\sum_i \sum_j k_{ij} / \sigma_s^2 \right] \right\}^{-1} = \frac{\sigma_s^2}{\Lambda_s} \quad (10a)$$

A similar derivation yields the lower bound for the variance of the y-coordinate estimate:

$$\text{var}(\hat{y}_0 - y_0) \geq \left\{ -E \left[-\sum_i \sum_j k_{ij} / \sigma_s^2 \right] \right\}^{-1} = \frac{\sigma_s^2}{\Lambda_s} \quad (10b)$$

where $\Lambda_s = E \sum_i \sum_j k_{ij}$ is the total signal energy collected by the detector array. It is apparent that the variance of the coordinate estimate for each dimension is directly proportional to the squared-spread of the PSF, σ_s^2 , and inversely proportional to the average number of photons passing through the receiver aperture. A MATLAB implementation of the ML estimation algorithm was used to evaluate performance. Figures 3(a) and 3(b) show the performance of the centroid algorithm for two different PSF spreads, using average signal counts consistent with the results of the Appendix, with small enough PSF and near enough the center of the detector array so that the large array assumption remained valid (the center of the array is at coordinates (8,8) for these numerical examples). The large dashed circle represents the standard deviation of the PSF, whereas the small solid circle is the Cramér-Rao bound expressed as the two-dimensional standard deviation of the lower bound on estimation error. Twenty independent estimates were made for each figure, shown by blue diamonds. Note that the cluster of estimates in Figure 3(b) is slightly biased towards the center of the array, because the PSF is larger and closer to the edge of the detector array, hence the assumption of a suitably large array is not strictly accurate.

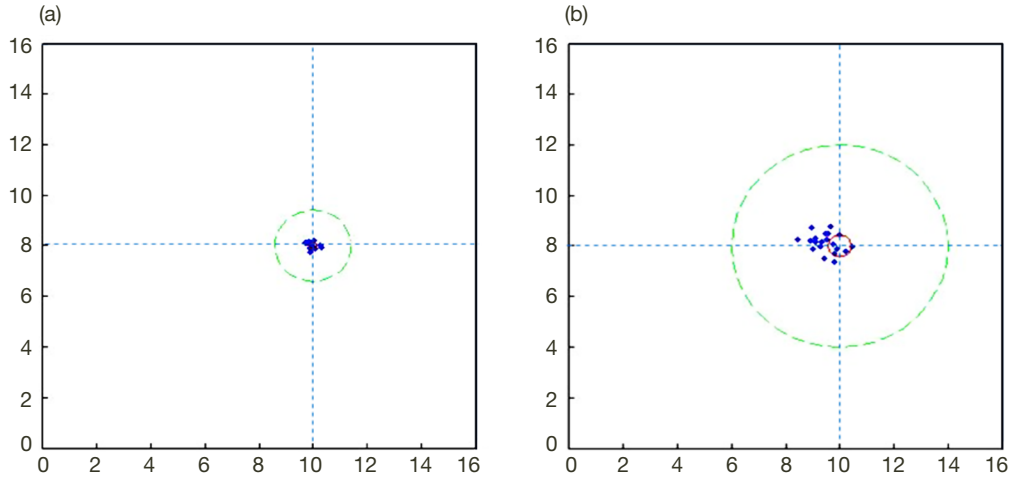


Figure 3(a). Centroid estimates at offset coordinates (10,8), with an average of 100 photons/pulse, $\sigma_s = 2$;
(b) same as (a) with $\sigma_s = 4$.

C. Finite Detector Array

Next, consider the modifications needed to accommodate a finite detector array; that is, one for which the sum of counts from all detector elements does not accurately represent the total number of photons passing through the receiver aperture (even after accounting for system transmission losses and detector quantum efficiencies). This modification is a first-order correction applied to the centroid algorithm, attempting to remove the bias resulting from the “edge-effect” of an insufficiently large detector array. Starting with the derivative of the log-likelihood function, now we do not ignore the term corresponding to the average number of photons through the aperture, and specifically include the functional form of the PSF:

$$\begin{aligned} \frac{\partial}{\partial x_0} \ln p(\mathbf{k} | x_0, y_0) &= \sum_{i,j} k_{ij} (i\Delta - x_0) / \sigma_s^2 - I_s \Delta^2 T (2\pi\sigma_s^2)^{-1/2} \sum_{i,j} \frac{(i\Delta - x_0)}{\sigma_s^2} \exp\{-(i\Delta - x_0)^2 \\ &\quad + (j\Delta - y_0)^2 / 2\sigma_s^2\} = 0 \\ \sum_{i,j} k_{ij} (i\Delta - x_0) &= I_s \Delta^2 T (2\pi\sigma_s^2)^{-1/2} \sum_{i,j} (i\Delta - x_0) \exp\{-(i\Delta - x_0)^2 + (j\Delta - y_0)^2 / 2\sigma_s^2\} \\ x_0 &= \frac{\sum_{i,j} k_{ij} i\Delta}{\sum_{i,j} k_{ij}} + \frac{I_s \Delta^2 T (2\pi\sigma_s^2)^{-1/2}}{\sum_{i,j} k_{ij}} \left\{ x_0 \sum_{i,j} \exp\{-(i\Delta - x_0)^2 + (j\Delta - y_0)^2 / 2\sigma_s^2\} \right. \\ &\quad \left. - \sum_{i,j} i\Delta \exp\{-(i\Delta - x_0)^2 + (j\Delta - y_0)^2 / 2\sigma_s^2\} \right\} \end{aligned} \quad (11)$$

This equality suggests the following two-step approach to correct the bias from the edge-effect:

- (1) Compute the centroid for both coordinates:

$${}_1\hat{x}_0 = \sum_i i k_i / \sum_{i,j} k_{ij} \quad {}_1\hat{y}_0 = \sum_j j k_j / \sum_{i,j} k_{ij}$$

- (2) Substitute the biased estimates into the right-hand side (RHS) of Equation (11) to obtain the first-order correction:

$$\begin{aligned} {}_2\hat{x}_0 &= {}_1\hat{x}_0 + \frac{I_s \Delta^2 T (2\pi\sigma_s^2)^{-1/2}}{\sum_{i,j} k_{ij}} \left\{ {}_1\hat{x}_0 \sum_{i,j} \exp\{-(i\Delta - {}_1\hat{x}_0)^2 + (j\Delta - {}_1\hat{y}_0)^2 / 2\sigma_s^2\} \right. \\ &\quad \left. - \sum_{i,j} i\Delta \exp\{-(i\Delta - {}_1\hat{x}_0)^2 + (j\Delta - {}_1\hat{y}_0)^2 / 2\sigma_s^2\} \right\} \end{aligned} \quad (12a)$$

$$\begin{aligned} {}_1\hat{y}_0 &= {}_1\hat{y}_0 + \frac{I_s \Delta^2 T (2\pi\sigma_s^2)^{-1/2}}{\sum_{i,j} k_{ij}} \left\{ {}_1\hat{y}_0 \sum_{i,j} \exp\{-(i\Delta - {}_1\hat{x}_0)^2 + (j\Delta - {}_1\hat{y}_0)^2 / 2\sigma_s^2\} \right. \\ &\quad \left. - \sum_{i,j} j\Delta \exp\{-(i\Delta - {}_1\hat{x}_0)^2 + (j\Delta - {}_1\hat{y}_0)^2 / 2\sigma_s^2\} \right\} \end{aligned} \quad (12b)$$

This process, described mathematically in Equations (12a) and (12b), can be repeated iteratively to obtain better estimates, if needed. However, the first order correction may be adequate for most communications applications, as the following numerical examples illustrate.

In Figures 4(a) and 4(b), the offset in the x-direction has been increased to 15, to bring it close to the simulated detector-edge at $x = 16$. Both centroid (red diamonds) and first-order corrected (blue asterisks) estimates are displayed. Note that the first-order corrected estimates are much closer to the true center of the PSF than the uncorrected centroid estimates, although it can be perceived that further improvements are possible to reduce the remaining small bias. The exact ML estimate will be examined next, which is equivalent to an arbitrarily high-order correction, hence should eliminate the remaining bias altogether.

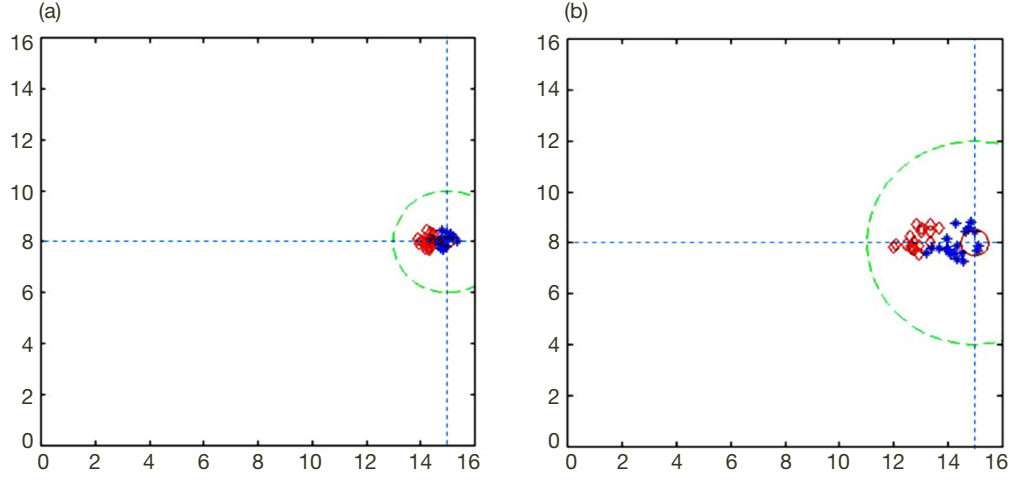


Figure 4(a). Centroid and first-order corrected estimates at offset coordinates (15,8) with an average of 100 photons/pulse, $\sigma_s = 2$; (b) same as (a) with $\sigma_s = 4$.

D. The Exact ML Solution, Without Background

Even without the presence of significant background radiation, the exact ML solution that takes into account the effects of realistic PSF dimensions over finite-detector arrays becomes somewhat complicated to describe and evaluate. Again, starting with the log-likelihood function and substituting for the specific form of the PSF, we differentiate with respect to each coordinate and set equal to zero to obtain a pair of equalities. The ML solutions are those values of (x_0, y_0) that simultaneously satisfy the following pair of equalities, where the ML estimates are denoted by $(_{ml}\hat{x}_0, _{ml}\hat{y}_0)$:

$$\sum_{i,j} k_{ij} (i\Delta - _{ml}\hat{x}_0) = I_s \Delta^2 T (2\pi\sigma_s^2)^{-1} \sum_{i,j} i\Delta - _{ml}\hat{x}_0 \exp\{ -[(i\Delta - _{ml}\hat{x}_0)^2 + (j\Delta - _{ml}\hat{y}_0)^2] / 2\sigma_s^2 \} \quad (13a)$$

$$\sum_{i,j} k_{ij} (j\Delta - _{ml}\hat{y}_0) = I_s \Delta^2 T (2\pi\sigma_s^2)^{-1} \sum_{i,j} j\Delta - _{ml}\hat{y}_0 \exp\{ -[(i\Delta - _{ml}\hat{x}_0)^2 + (j\Delta - _{ml}\hat{y}_0)^2] / 2\sigma_s^2 \} \quad (13b)$$

The method of solution requires the estimator to substitute trial values for the estimates in some predetermined manner, and converge on those values that achieve equality. Since the estimates are uncoupled, we can start by first determining either the “centroid” or “corrected centroid” estimates, defining uncertainty regions around them via a priori predictions, and applying one of these approximate values for the orthogonal parameter that is not being maximized (that is, use the centroid estimate for the y-coordinate when maximizing the log-likelihood function for the x-coordinate, and vice versa). Because of the assumed circular symmetry of the PSF, a slightly inexact value of the orthogonal component will not impact the ML estimate significantly. After obtaining the true ML estimate of the x-coordinate, this value is then substituted into the second equation when solving for the ML estimate of the y-coordinate.

The following two-step procedure assumes that $_{ml}\hat{x}_0$ is being solved for:

- (1) Determine the approximate centroid solution, \hat{y}_0 , and use this value in the RHS of Equation (13a) to determine $_{ml}\hat{x}_0$ by varying x_0 around \hat{x}_0 .
- (2) Substitute the value of $_{ml}\hat{x}_0$ so obtained into the RHS of Equation (13b) and solve for $_{ml}\hat{y}_0$.

This approach was implemented in MATLAB to generate Figures 5(a) and 5(b). Initially, an uncertainty region was defined that contained the true solutions. The centroid estimate of the orthogonal component was then obtained to serve as an initial guess, and substituted to facilitate the solution via the above two-step process. The RHS was then subtracted from the left-hand side (LHS), and the test-value stepped through the region until a zero-crossing was observed. Linear interpolation was used to obtain the zero-crossing, which was then declared to be the ML estimate of x_0 .

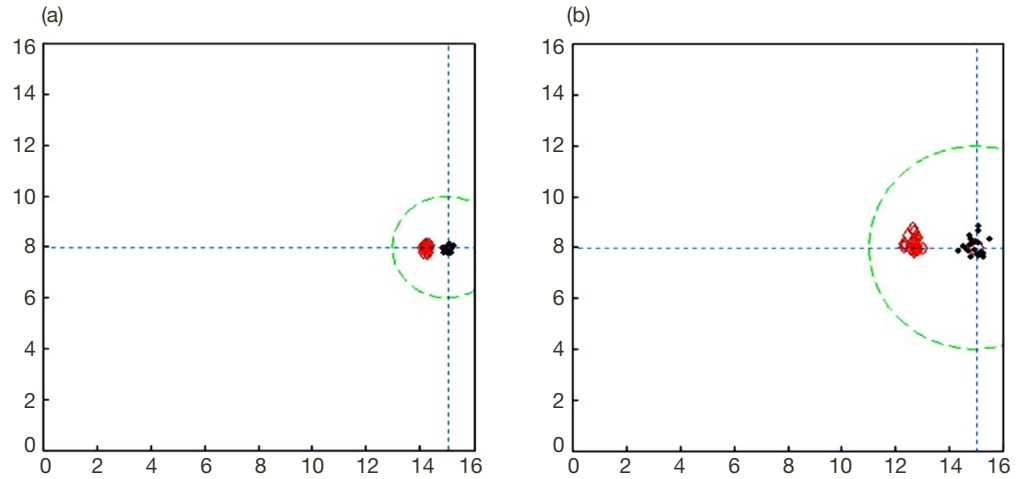


Figure 5(a). Centroid and ML estimates at offset coordinates (15,8) with an average of 100 photons/pulse, $\sigma_s = 2$; (b) same as (a) with $\sigma_s = 4$.

V. Temporal Acquisition of the Centered PSF with a Timing Offset

After successful spatial acquisition, it is assumed that a closed-loop tracking system will be activated (using the array outputs for tracking, possibly partitioned via signal processing to serve as a quadrant detector), and keep the PSF centered over the detector array. Since by design there is sufficient signal energy to enable communication at a high rate (1 GBPS is the goal), it can be argued that the SNR within the much narrower (typically 1 Hz to 3 Hz) closed-loop bandwidth will be more than sufficient to continue spatial tracking of the PSF under nominal operating conditions. Therefore, we will not pursue the details of the spatial tracking system design here, concentrating instead on the analysis of the temporal acquisition problem.

Temporal acquisition is inherently a one-dimensional problem, requiring only the estimation of a single delay instead of two orthogonal spatial offsets. This simplification provides an opportunity to start considering the effects of background radiation, which is now included in the model as a constant average power P_b in Figure 6. We model the laser pulse as a one-dimensional Gaussian distribution matched to the slot-duration, to facilitate analysis closely paralleling the spatial acquisition problem investigated previously. This pulse-shaping approximation yields a Gaussian distribution for the frequency spectrum, enabling approximate assessment of the spectral requirements for this signal. The temporal distribution is of the form $P_s(t|\tau) = P_s(2\pi\sigma_t^2)^{-1/2} \exp\{-(t-\tau)^2/2\sigma_t^2\}$, where σ_t^2 is the effective spread of the pulse and τ is the offset we need to estimate. It is assumed at this point that all of the signal photons collected by the focal-plane detector array are available to the temporal acquisition algorithm: therefore, the units of the average signal and background variables are watts (intensity integrated over detector area), and the average signal and background photon-counts for a time-sample are obtained by integrating power over time:

$$\lambda_s(i|\tau) = \int_{(i-1)\delta}^{i\delta} P_s(i|\tau) dt = \Lambda_s \delta / T \quad \lambda_b(i) = \int_{(i-1)\delta}^{i\delta} P_b dt = \Lambda_b \delta / T$$

In our model, the sample-duration is δ , hence there are T/δ samples per T -second slot: in the simulations, we assume that $T/\delta = 4$. We first assume zero background, then incorporate background effects into the model and the solution. The delay-estimation algorithm will then be extended to the two-dimensional spatial acquisition of the PSF, in the presence of background.

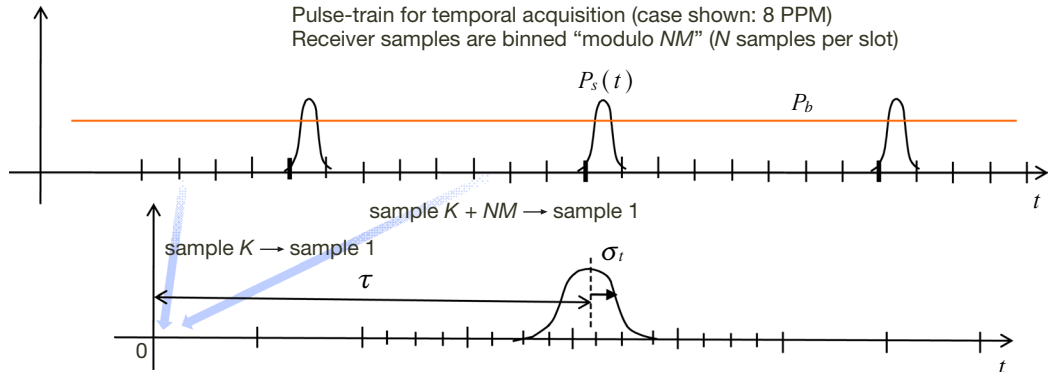


Figure 6. Temporal acquisition via known pattern of PPM symbols, binned modulo NM to create a single pulse.

A. No Background, Large Detector Array

In the absence of background, the temporal log-likelihood function becomes

$$\begin{aligned}\ln p'(\mathbf{k}|\tau) &= \ln \left\{ \prod_i [\lambda_s(i)]^{k_i} \exp[-\lambda_s(i)/k_i!] \right\} \\ &= \sum_i k_i \ln[\lambda_s(i)] - \sum_i \lambda_s(i) \quad \mathbf{k} = (k_1, k_1, \dots, k_N) \\ &= -\sum_i k_i (i\delta - \tau)^2 / 2\sigma_i^2 - \frac{\Lambda_s}{\sqrt{2\pi\sigma_i^2}} \sum_i \exp[-(i\delta - \tau)^2 / 2\sigma_i^2]\end{aligned}$$

Differentiating and equating to zero,

$$\begin{aligned}\frac{\partial}{\partial \tau} \ln p'(\mathbf{k}|\tau) &= -\sum_i k_i \frac{\partial}{\partial \tau} (i\delta - \tau)^2 / 2\sigma_i^2 \\ &= \sum_i k_i (i\delta - \tau) / \sigma_i^2 = 0\end{aligned}$$

Solving, this yields

$$\hat{\tau} = \delta \sum_i k_i i / \sum_i k_i$$

As before, the algorithm reduces to a centroid estimator for delay, when the form of the shaped laser pulse is assumed to be Gaussian. Substituting delay for the spatial offset and using the standard deviation appropriate for the time-slots, the performance of this estimator is again bounded by the Cramér-Rao bound (CRB): $\text{var}(\hat{\tau} - \tau) = \sigma_i^2 / \Lambda_s$. As before, estimator variance is proportional to pulse-spread, and inversely proportional to collected signal energy.

B. Strong Background, Large Detector Array

When strong background is present, the background intensity must be incorporated into the likelihood function. Replacing $\lambda_s(i)$ with $[\lambda_s(i) + \lambda_b]$ everywhere, and further assuming that $\lambda_b \gg \lambda_s(i) \forall i$, the following approximate log-likelihood function is obtained:

$$\begin{aligned}\ln p(\mathbf{k}|\tau) &= \ln \left\{ \prod_i [\lambda_s(i) + \lambda_b]^{k_i} \exp\{-[\lambda_s(i) + \lambda_b]\} / k_i! \right\} \\ \ln p'(\mathbf{k}|\tau) &= \sum_i k_i \ln[\lambda_s(i) + \lambda_b] - \sum_i [\lambda_s(i) + \lambda_b] \\ &= \sum_i k_i \ln \left\{ \frac{\Lambda_s \delta / T}{\sqrt{2\pi\sigma_i^2}} \exp[-(i\delta - \tau)^2 / 2\sigma_i^2] + \Lambda_b \delta / T \right\} \\ &= \sum_i k_i \ln(\Lambda_b \delta / T) + \sum_i k_i \ln \left\{ \frac{\Lambda_s}{\Lambda_b \sqrt{2\pi\sigma_i^2}} \exp[-(i\delta - \tau)^2 / 2\sigma_i^2] + 1 \right\} \\ &\stackrel{\Lambda_b \gg \Lambda_s}{\cong} \sum_i k_i \ln(\Lambda_b \delta / T) + \frac{\Lambda_s}{\Lambda_b \sqrt{2\pi\sigma_i^2}} \sum_i k_i \exp[-(i\delta - \tau)^2 / 2\sigma_i^2]\end{aligned} \tag{14}$$

where we made use of the approximation $\ln(1+x) \stackrel{x \ll 1}{\cong} x$. Differentiating with respect to τ and setting equal to zero to find the maximum, we obtain

$$\frac{\partial}{\partial \tau} \ln p'(\mathbf{k}|\tau) = \frac{\Lambda_s}{\Lambda_b \sqrt{2\pi\sigma_i^2}} \sum_i k_i (i\delta - \tau) \exp[-(i\delta - \tau)^2 / 2\sigma_i^2] = 0$$

yielding

$$\tau \sum_i k_i \exp[-(i\delta - \tau)^2 / 2\sigma_i^2] = \delta \sum_i ik_i \exp[-(i\delta - \tau)^2 / 2\sigma_i^2]$$

The last equality suggests that different values of τ might be tried and refined until equality is obtained. Therefore, the estimate of τ is that value, $\hat{\tau}$, that satisfies the above equality within some predetermined error tolerance. A convenient form of this algorithm for MATLAB simulation is obtained when we subtract the RHS from the LHS, and search for a zero-crossing numerically:

$$\hat{\tau} \sum_i k_i \exp[-(i\delta - \hat{\tau})^2 / 2\sigma_i^2] - \delta \sum_i ik_i \exp[-(i\delta - \hat{\tau})^2 / 2\sigma_i^2] = 0 \quad (15)$$

Although derived for the case of strong background, the above algorithm for estimating τ was found to work best with a strong signal and weak background, improving significantly over the centroid algorithm, which is optimum in the absence of background. One reason for the difficulty in estimating the offset for pulses near the M -th slot (regardless of where we start counting) is that in the proposed algorithm there is signal wraparound into the first few slots, which is an edge-effect that was not modeled in the likelihood function. However, wraparound was incorporated into the simulation at the upper boundary by adding in the counts that would have occurred in slots past the upper boundary, into the corresponding slots at the beginning of the observation interval, modulo M . Since wraparound was implemented at the upper boundary, the algorithms should only be tested at offsets at and above the center of the interval (that is, $8 \leq \tau \leq 15$). When $\tau = 16$, the near-optimum algorithm tends to choose between 0 and 16 with equal probability.

The center of the interval is at $M = 8$, at greatest distance from both edges, where edge-effects are the least significant and hence we expect best performance in this region. Twenty independent estimates were made using the centroid algorithm (dashed red lines) and the near-optimum solution (solid blue line) in Figures 7 and 8. With average signal energy

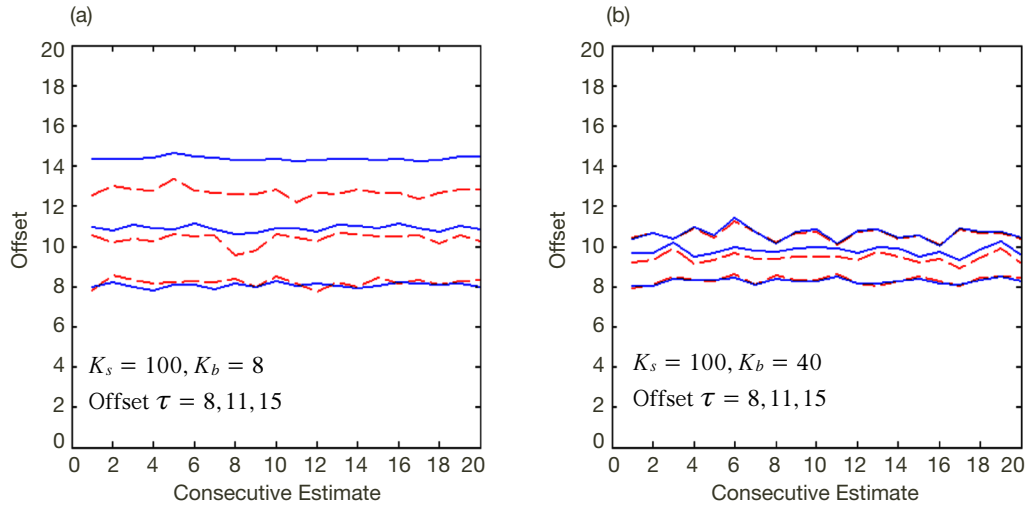


Figure 7. Near-optimum delay estimator (solid blue) and centroid estimator (dashed red) performance over 20 consecutive estimates, for offsets of 8, 11, and 15 samples, with $K_s = 100$ photons per pulse:

(a) $K_b = 8$; (b) $K_b = 40$.

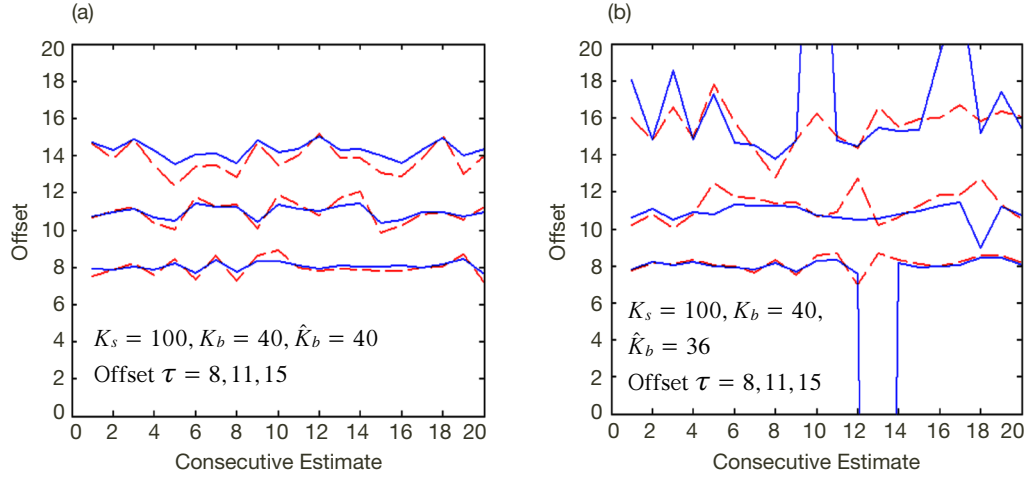


Figure 8. Near-optimum delay estimator and centroid estimator (dashed red) performance for offsets of 8, 11, and 15 samples, with $K_s = 100$ signal photons per pulse and $K_b = 40$: (a) exact background level subtracted; (b) background estimate with 10 percent error subtracted.

of 100 photons (again consistent with the results of the Appendix) and background of only 8 photons per slot, both the centroid and the near-optimum estimates are of similar quality when the true offset is $\tau = 8$; however, the centroid estimator underestimates the offset when $\tau = 11$ and 15 in Figure 7(a). The reason is that the center of mass of the constant background distribution is at the center of the PPM symbol, hence the centroid estimator is biased towards the center of the estimation interval when background is present.

The near-optimum estimator solves this problem by weighting the observed counts according to the Gaussian pulse model, which tends to suppress the background on the tails of the distribution, but emphasizes the signal near the true delay to compute a more accurate estimate. Only when edge-effects begin to dominate, near the edge of the interval, does the near-optimum algorithm begin to underestimate the delay, since edge-effects have not been incorporated into the log-likelihood function as stated earlier.

With the higher background level of 40 photons per slot shown in Figure 7(b), both estimators fail to overcome the background sufficiently and underestimate the true delay near the edge: for $\tau = 8$, both estimators are accurate, but for $\tau = 11$ the estimates are close to 10 (somewhat lower for the centroid estimator), but both estimators fail when $\tau = 15$, yielding estimates between 10 and 11, which is strongly biased towards the center.

It is natural to ask whether subtracting out the background would remedy this situation, effectively eliminating the large constant background distribution that biases the centroid and near-optimum estimators, leaving only zero-mean fluctuations that should not bias the estimators towards the center. This idea was explored by subtracting a constant from the counts corresponding to the mean value of the background, assuming that the true value could be estimated accurately. However, since perfect estimates of the background are generally not available, errors in the estimate of the mean were also considered. The results are shown in Figures 8(a) and 8(b). It is immediately apparent in Figure 8(a) that the mean of the estimates for both the centroid and the near-optimum estimators improved to

8, 11, and 14 (instead of the true value of 15) when a perfect estimate of the background level (40 photons per slot) was subtracted out before processing; however, the scatter in the estimates also increased noticeably. When the estimate of the background level is not known with perfect accuracy, as is generally the case, the scatter of the centroid estimator increases still further, while the near-optimum estimator becomes unstable and outliers begin to occur even for offsets near the center of the interval, as shown in Figure 8(b), where a background level of 9 was subtracted out instead of the true value of 10, representing a 10 percent error in knowledge of the background level.

C. Returning to the Centroid Estimator of Spatial Offset in the Presence of Background

Although the true ML estimator of spatial offset in the presence of background is not considered here due to its complexity, we observe from the temporal acquisition problem that subtracting the mean background from each detector element helps to remove the bias caused by uniformly distributed background intensity over the detector array. Because the background energy is uniformly distributed over the detector plane, it tends to bias the centroid estimate towards the center of the array, as illustrated in Figures 9(a) and 9(b): with true offset coordinates of (13,13) and with a small spotsize so that edge-effects are not significant, the addition of background counts shifts the centroid estimates towards (8,8), which is the center of the detector array. This shift can be eliminated by subtracting out the average background count from the array observable, leading to nearly unbiased estimates as shown in Figure 9(a) (blue dots); however, the variance of the estimates increases significantly due to the large random distribution of counts around their mean value across the array. Note that any error in the estimate of the average background leads to both increased variance and bias, as shown in Figure 9(b), where the mean background counts subtracted from each detector are in error by 10 percent. The resulting estimation variance can be further reduced by averaging a large number of independent estimates; however, the bias term

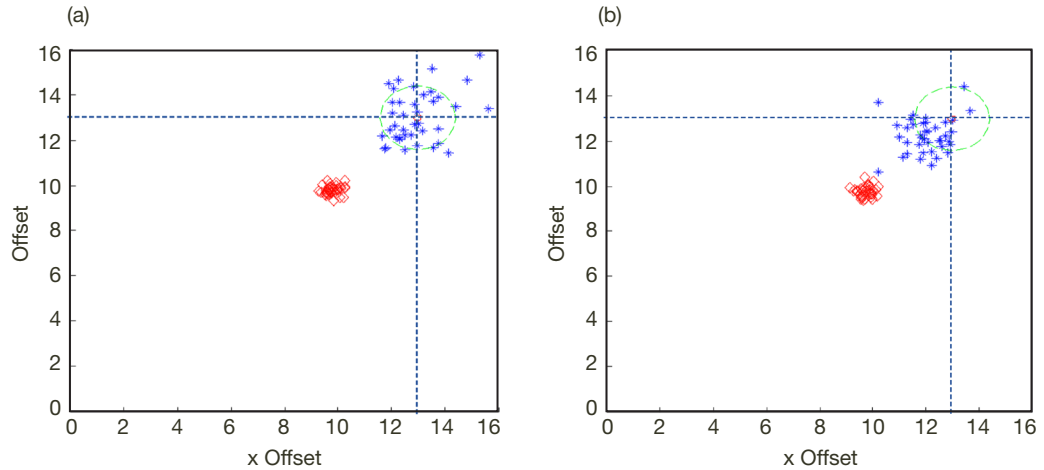


Figure 9. Centroid estimates without removing average background (red diamonds), and with average background level removed (blue asterisks) at offset coordinates (13,13), with an average of 100 signal photons and 1 background photon per detector element $\sigma_s = 2$: (a) background level known exactly; (b) background level underestimated by 10 percent.

is not reduced by averaging. Therefore, it is important to obtain accurate estimates of the average background before subtraction to avoid steering the receiver pointing away from the true source direction due to the induced bias.

VI. Optimized-FOV ML Detection of PPM Symbols

Following successful spatial and temporal acquisition, we can assume that the PSF is kept centered over the detector array (whose dimensions are initially taken to be large enough to capture all of the signal energy) by means of a closed-loop tracking circuit. Temporal acquisition and tracking is also assumed, meaning that the receiver clock has been successfully synchronized with the slot boundaries. Under these conditions, the receiver FOV can be optimized to achieve best detection performance by increasing the acceptance angle of the receiver in small increments, and computing the PPM symbol-error probability for each increasing radius R in the detector plane, proportional to linear FOV. This is the scenario depicted in Figure 10, where the PSF and hence the FOV are assumed to be circular. The signal distribution is taken to be circular Gaussian as before, with spread equal to σ_s .

The amount of signal energy collected by a circular FOV of radius R can be calculated as

$$\begin{aligned} \frac{1}{2\pi\sigma_s^2} \int_0^R 2\pi r \exp[-r^2/2\sigma_s^2] dr &= - \int_0^R \frac{r}{\sigma_s^2} \exp[-r^2/2\sigma_s^2] dr \\ &= \exp[-r^2/2\sigma_s^2] \Big|_R^0 = 1 - \exp[-R^2/2\sigma_s^2] \end{aligned}$$

Note that in the limit as R approaches infinity, all of the signal energy is captured, according to the Gaussian PSF model. Therefore, $\lim_{R \rightarrow \infty} \Lambda_s(R) = K_s$, where K_s is the total signal energy per pulse, measured in terms of photon energy, passing through the receiver aperture.

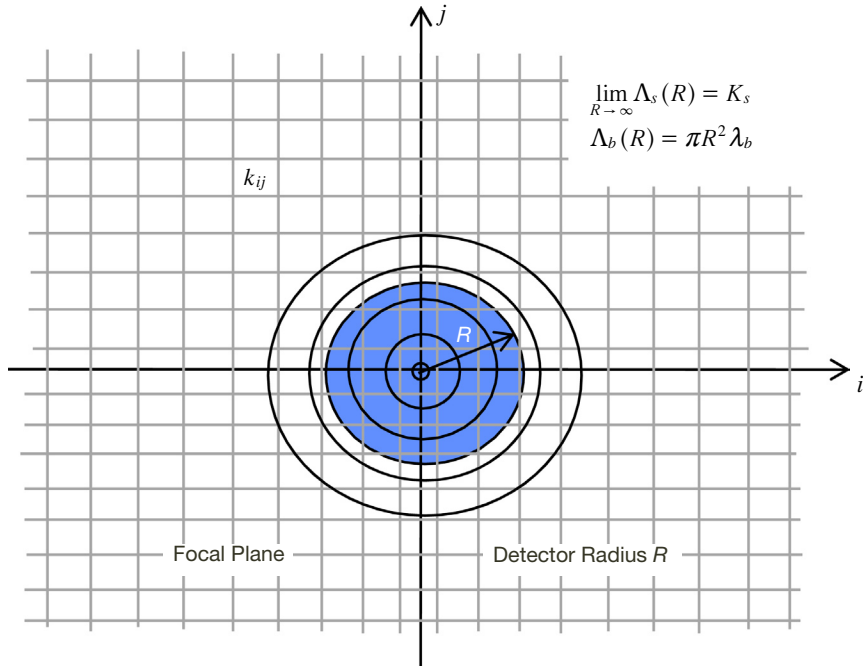


Figure 10. Receiver FOV optimization via the radius of the acceptance-disk in the detector plane.

However, the background photon distribution is assumed to be uniform in the detector plane, hence the collected background energy increases with R in proportion to the area of the circular FOV, therefore, there is no limit to the amount of background energy that can be collected by the receiver according to this model: $\Lambda_b(R) = \pi R^2 \lambda_b$, where λ_b is the average background photon count per square centimeter in the detector plane.

Consider the probability of correct symbol detection, with PPM signaling. For any R , the probability of correct symbol detection is at least as great as the probability that the photon count in the correct slot (containing the signal pulse) exceeds the count in every other slot. To be more precise, tying equalities in $(r-1)$ noise slots ($1 < r < M$) should also be considered and resolved by tossing a fair r -sided die, but with high average signal and background energies these events have extremely small probabilities, hence can be neglected. With this approximation, the lower bound on the probability of correct decision, $P_M^l(C)$, as a function of R is given by

$$P_M^l(C) \geq \sum_{k=1}^{\infty} \frac{(\Lambda_s(R) + \Lambda_b(R))^k}{k!} \exp[-(\Lambda_s(R) + \Lambda_b(R))] \left\{ \sum_{j=0}^{k-1} \frac{(\Lambda_b(R))^j}{j!} \exp[-(\Lambda_b(R))] \right\}^{M-1} \quad (16)$$

$$P_M^u(E) \equiv 1 - P_M^l(C) \geq P_M(E) \cong P_M(E)$$

The corresponding symbol error probability, $P_M(E)$, is actually somewhat less than predicted by this approach, but not significantly so. Further simplifications are possible by resorting to a Gaussian approximation, which is generally valid for high signal and background intensities:

$$P_M(C) \cong \int_{-\infty}^{\infty} dy Gsn[\Lambda_s(R) + \Lambda_b(R), y] \left[\int_{-\infty}^y dx Gsn[\Lambda_b(R), x] \right]^{M-1} \quad (17)$$

$$P_M(E) = 1 - P_M(C)$$

A direct comparison of the Poisson and Gaussian computations showed that both yield very similar results for the region of signal and background intensities of interest. However, the Gaussian approximation is much faster computationally, hence will be used throughout the rest of the article.

A. Performance of the 26-m “Polished-Panel” Receiver

We first evaluate the performance of the 26-m “polished-panel” receiver described in Section II. The performance optimization, which is actually a minimization of the symbol error probability $PSE(R)$ as a function of detector radius R , was carried out numerically using an accurate Gaussian approximation to the Poisson probabilities. The radius was increased in small increments, and signal and background energies as well as $PSE(R)$ were computed for each radius. The variation of signal and background energies for PSF spreads of approximately 2, 3, and 4 cm is shown in Figure 11(a) (corresponding to $\sigma_{PSF} = 1, 1.5$, and 2 cm, with the corresponding symbol-error probabilities shown in Figure 11(b). As expected, performance is best for the smallest PSF, since this allows collection of the signal energy with

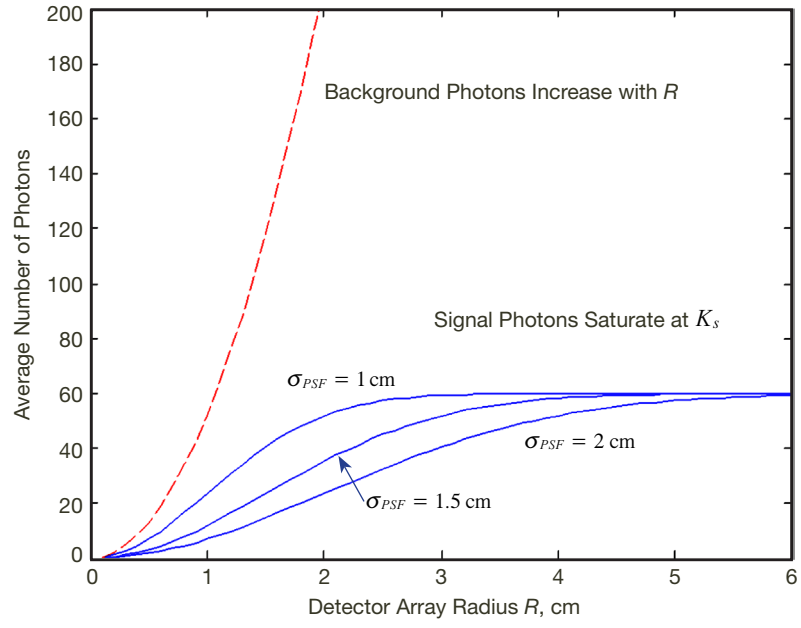


Figure 11(a). Average signal and background energies as a function of acceptance radius (cm) in the detector plane for 2-, 3-, and 4-cm signal spots (1.25 AU).

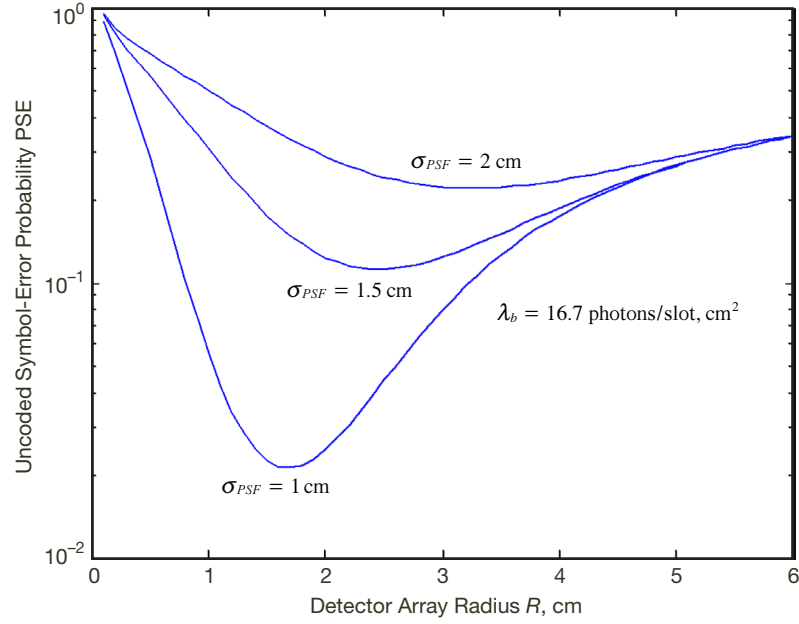


Figure 11(b). Example of symbol error probability optimization with 2-, 3-, and 4-cm signal spot (1.25 AU).

minimal background. Performance deteriorates by more than an order of magnitude as the PSF spread is increased from 1 to 2 cm (corresponding to 220 and 440 μrad , respectively, when the antenna's effective focal length is 91 m, as is the case for the DSN 34-m research antenna at Goldstone), emphasizing the importance of reducing the PSF, hence the receiver FOV in communications applications.

Performance of a hypothetical 26-m optical photon-counting receiver utilizing the inner solid panels of an operational 34-m antenna is shown in Figure 11 for the following system parameters: 50 cm transmitting optics, 10 W of transmitted laser power (20-W laser with 50 percent efficiency through the transmitting optics), and 26-m receiver corresponding to 531 square meters of aperture, and background radiation evaluated at a hypothetical Sun–Earth–probe (SEP) angle of 10 deg (this value is used only to provide a constant scattered background level for the numerical examples, and does not necessarily account for orbital geometry constraints of Mars or any other planet).

In addition, PSF standard deviation of $\sigma_{PSF} = 1$ cm, and optical system throughput of 0.324 was assumed, which includes main reflector and subreflector losses (90 percent reflectivity on each surface), optical filter transmission losses (assumed to be 80 percent transmission for a 2-Å optical filter at 1550 nm), as well as 50 percent detector quantum efficiency. Performance was determined as a function of R for the nominal range of 1.25 AU, as well as 0.87, 1.8, and 2.5 AU, using the nominal value of 93 photons/ns for the received signal photon intensity as derived in the Appendix. For PPM with $M=4$ and 0.5-ns slots, this yields approximately 60 photons/pulse from a distance of 1.25 AU, when 50 cm transmitter optics, 20-W laser, and 50 percent telescope transmission are assumed. Figure 12(a) shows the uncoded symbol error probability as a function of detector radius R . Figure 12(b) shows the increase of collected signal and background energies as a function of R : note that optimum performance occurs at 1.75 cm acceptance radius for all cases considered in Figure 12.

It can be seen in Figure 12(a) that while uncoded performance may be marginally acceptable at closest approach, the symbol error probability decreases rapidly at greater distances, since it is inversely proportional to the square of the distance. At the nominal distance of 1.25 AU, the symbol error probability is no longer acceptable for data reception, having degraded to approximately $PSE = 0.02$. Therefore, at all but the closest distance considered, some form of error-correction coding will be necessary to achieve the required error probabilities with the 26-m design.

Examples of the performance improvement afforded by coding are shown in Figure 13, where a 2-cm spot was assumed, and uncoded bit error rate (BER) as well as the BER for two coded systems are shown: one a rate 1/2 code, the other a rate 7/8 code. The rate 1/2 code is a (15120,7558) serially concatenated convolutional PPM code, whereas the rate 7/8 code is a (8176,7154) low-density parity-check (LDPC) code currently proposed as a Consultative Committee for Space Data Systems (CCSDS) standard high-rate code. Each of these codes utilizes iterative demodulation of the PPM symbols, providing an additional gain of approximately 0.2 dB. Both of these codes have been implemented in field-programmable gate array (FPGA), hence represent practical implementations that can be used with confidence to predict coded performance of the proposed optical receivers.

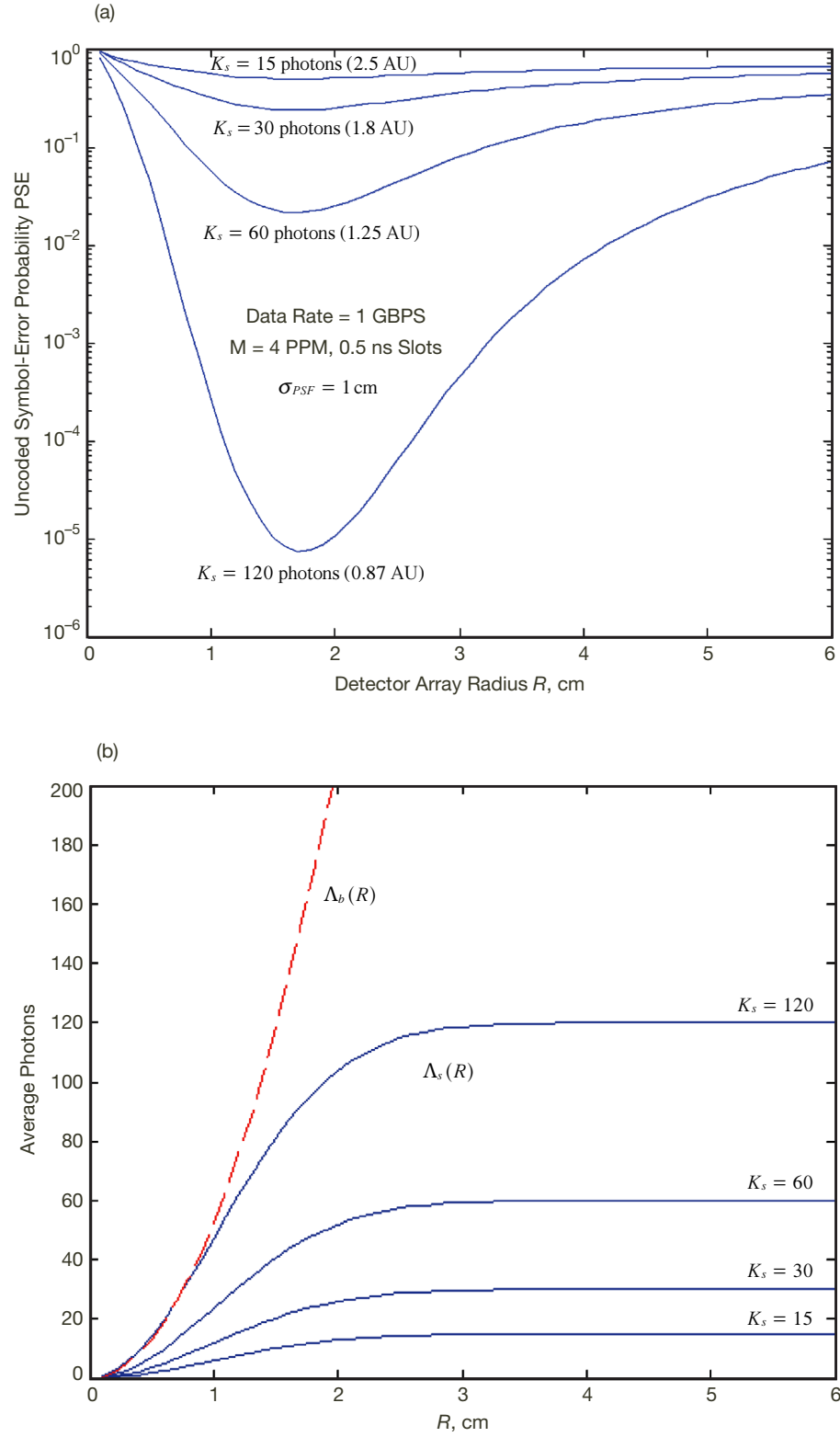


Figure 12(a). Uncoded symbol-error probability performance of 26-m receiver as a function of detector plane acceptance radius R at distances of 0.87, 1.25, 1.8, and 2.5 AU: approximately 2-cm spot;
(b) average signal and background intensities as a function of R .

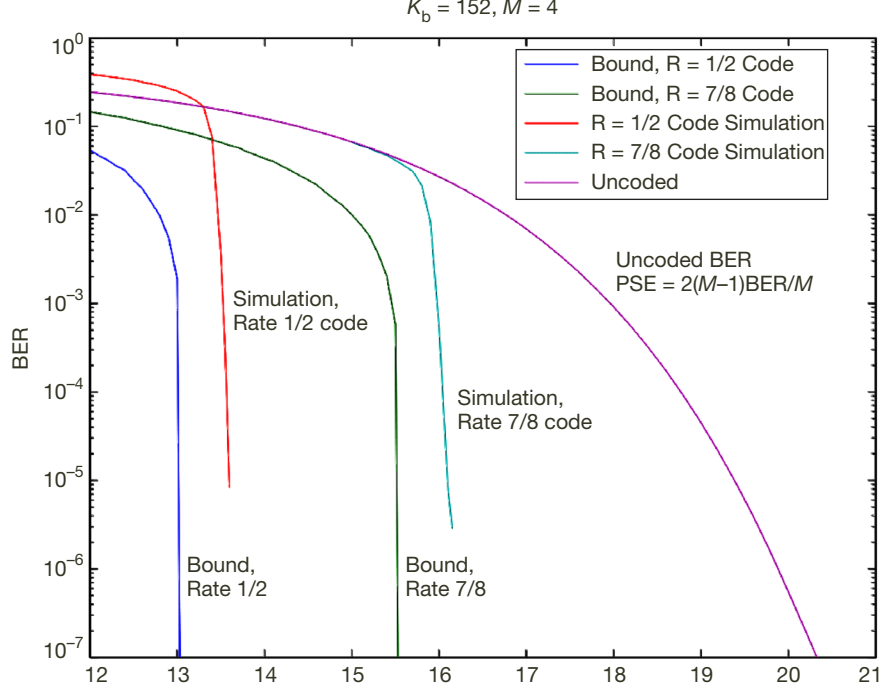


Figure 13. Coded performance of $M = 4$ PPM with background level corresponding to optimized acceptance angle for 2-cm spot, rate 1/2 and 7/8 codes.

It is evident that the more powerful rate 1/2 code attains 7-dB coding gain over uncoded BER at error probabilities of interest to missions ($BER \approx 10^{-6}$), but that even a rate 7/8 code provides more than 4 dB of coding gain. Also illustrated are bounds (sometimes referred to as capacity bounds) on the BER derived from the converse to the coding theorem for rates 1/2 and 7/8. These provide a lower bound on achievable error probability for any coding scheme at a given rate.

Note that a simulated rate 7/8 code would require an average of more than 16 photons to reach $BER \approx 10^{-6}$. With only about 15 signal photons received at the greatest distance of 2.5 AU as shown in Figure 12, the required BER of approximately 10^{-6} for communications links cannot be achieved with this high-rate code. In this case, a lower code rate could be used, but at the cost of additional overhead. The threshold of the simulated rate 1/2 code is less than 14 signal photons per pulse on the average in this high-background environment (152 background photons per slot at 10-deg SEP angle), hence this code could achieve the required BER with a 26-m receiver even at the greatest distances considered.

B. Performance of the 10-m Glass Optics Receiver

Finally, we consider the 10-m receiver option described in Section II. The salient characteristics of this receiver design are smaller turbulence-limited FOV due to higher-quality glass optics, but also a much smaller collecting area of only 78.5 square meters. Therefore the 10-m receiver collects a fraction $78.5/531 = 0.148$ of the signal power collected by the 26-m

antenna, corresponding to 8.3 dB less signal energy. However, due to higher-quality optics, the FOV can be reduced to 55 μrad (roughly the turbulence-induced limit at 10-deg SEP angle), yielding an effective spotsize of 0.5 cm at the Cassegrain focus. The distribution of background intensities in the focal plane have been scaled by the ratio of the apertures for the two options, enabling direct comparison of optimized performance.

Uncoded performance of the 10-m receiver design is shown in Figure 14, for spacecraft distances of 0.87, 1.25, 1.8, and 2.5 AU, respectively. At the nominal distance of 1.25 AU, three performance curves with slightly different spot sizes are plotted on the same graph: red corresponds to $\sigma_{PSF} = 0.2$, blue to 0.25, and green to 0.3 cm. It is noteworthy that not much background is collected with any of these spots to begin with, hence performance cannot be improved significantly by reducing the spotsize for the 10-m receiver option.

It should also be noted that the uncoded error probabilities achieved by the 10-m receiver are not quite as good as those of the 26-m receiver at any distance, despite much better optical surface quality: this is a direct consequence of the 8.3 dB loss in relative signal energy. However, since the background energy at minimum symbol error probability is only about 2 photons on the average per slot, coded performance nevertheless remains acceptable at moderate distances, as shown in Figure 15.

For the 10-m receiver, the threshold for the rate 1/2 code is approximately 5 signal photons on the average and a little more than 8 photons for the rate 7/8 code, which means that acceptable performance can be achieved at intermediate distances of 1.25 AU or less with either code.

However, if the less powerful rate 7/8 code was employed, then the required performance could not be achieved at distances much greater than 1.25 AU, since more than 8 photons would be required to reach the coding threshold, which, however, is not feasible with the 10-m receiver design, as can be seen in Figure 14.

VII. Summary and Conclusions

We have presented two different system concepts for hybrid RF/optical receivers based on the DSN 34-m antennas currently employed for deep-space communications. Although significantly different in terms of optomechanical design, the key features of these two concepts can be characterized as follows: the 10-m option utilizes high-quality glass mirrors added to the main reflector of the 34-m antenna to achieve an equivalent collecting aperture of a 10-m-diameter optical receiver, with a narrow FOV consistent with daytime turbulence when pointing close to the Sun (approximately 55 μrad); the 26-m option makes use of the existing solid aluminum panels of the inner 26 m of the antenna polished to optical smoothness, and is assumed to achieve a wider FOV of 200 to 400 μrad due to larger surface figure errors.

A mathematical model of the optical communications system applicable to both concepts was developed, consisting of a focal-plane array of photon-counting detectors, optical filter to limit background, and point-spread functions in the focal plane incorporating the

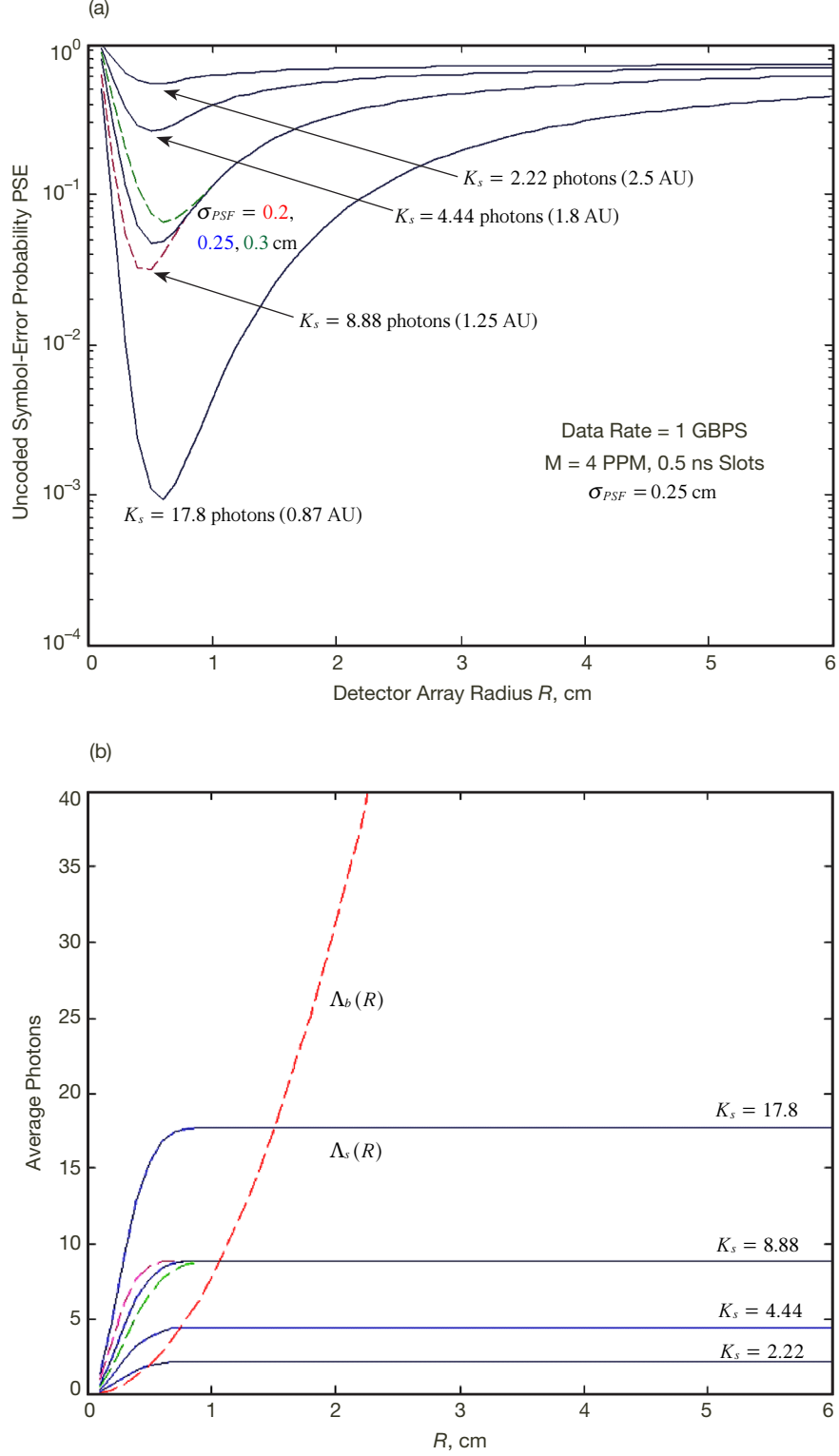


Figure 14(a). Unencoded symbol-error probability performance of 10-m receiver as a function of detector plane acceptance angle, at distances of 0.87, 1.25, 1.8, and 2.5 AU: approximately 0.4-, 0.5-, and 0.6-cm spots; (b) average signal and background intensities as a function of R .

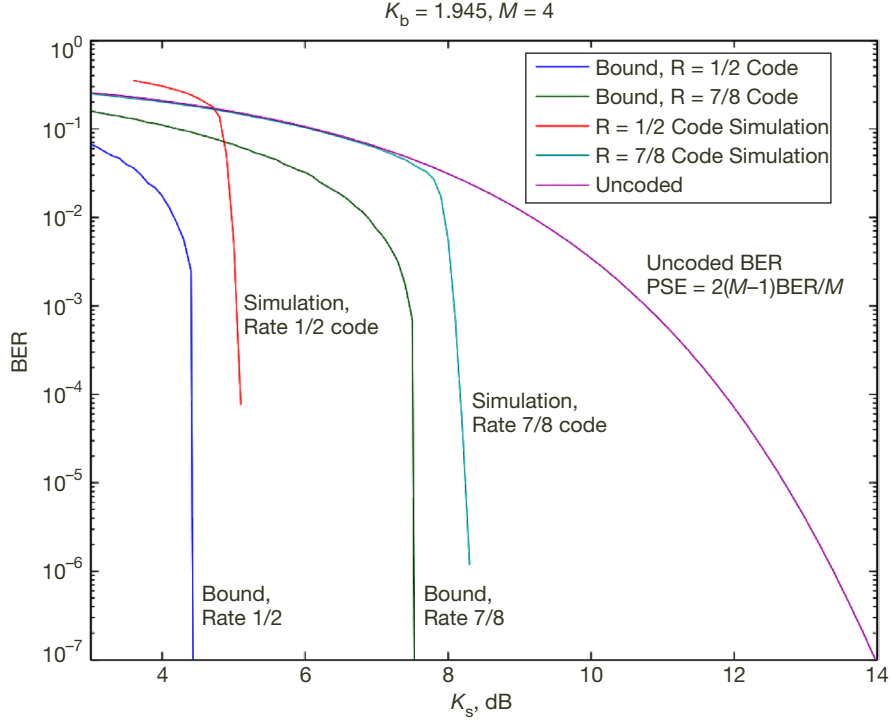


Figure 15. Coded performance of $M = 4$ PPM with background level corresponding to optimized acceptance angle for 0.5-cm spot, rate 1/2 and 7/8 codes.

surface figure errors of the two concepts. Both spatial and temporal acquisition algorithms were considered, and it was shown that in the absence of background radiation and with large detector arrays the ML estimators took the form of simple centroiding operations. When the detector array was comparable in size to the PSF, then edge-effects had to be considered, and several modifications were derived that ameliorated the bias caused by these edge-effects.

It was also found that uniformly distributed background introduced large biases into the centroid estimates for both pointing offset and temporal delay, requiring modifications to the original algorithms to overcome these effects.

Finally, detector FOV was optimized for both design concepts to minimize PPM symbol-detection error probability in the presence of strong background, characteristic of daytime operation when pointing close to the Sun. Uncoded performance was evaluated assuming $M = 4$ PPM and 1 GBPS data rate, and it was shown that the 26-m collecting aperture outperformed the 10-m aperture despite its narrower FOV, since the larger aperture collected many more signal photons. Coded performance was also considered with optimized FOV, demonstrating that acceptable coded performance could be achieved with either design for communications distances characteristic of nearby planets.

Acknowledgments

The author would like to thank Bruce Moision for generating the coded performance curves of Figures 13 and 15, and explaining their characteristics; and Sabino Piazzolla for determining the effective sky radiance at 10-deg SEP angle due to atmospheric scattering and dust on the optics, used in the calculations in Section VI.

References

- [1] R. Gagliardi and S. Karp, *Optical Communications*, New York: John Wiley and Sons, 1976.
- [2] V. Vilnrotter and M. Srinivasan, "Adaptive Detector Arrays for Optical Communications Receivers," *IEEE Transactions on Communications*, vol. 50, issue 7, July 2002.

Appendix

The intensity distribution a distance z from the transmitting telescope is computed, assuming the telescope is a folded design with a central obstruction. The problem formulation is shown in Figure A-1, where circular symmetry is assumed in both the transmitter and receiver planes.

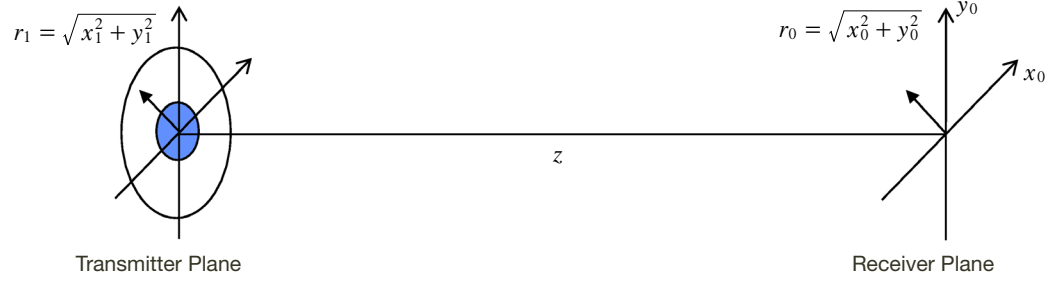


Figure A-1. Coordinate systems defining transmitter-plane and receiver-plane geometries.

The received field $U(r_0)$ is modeled as the Fourier-Bessel transform of the transmitted field distribution, $U(r_1)$, which includes the central obstruction. Proper normalization of the field amplitude is required to ensure that the total laser power passing through the obstructed aperture is P watts. With $k = 2\pi/\lambda$, the received field can be expressed as

$$U(r_0) = \sqrt{\frac{P}{\frac{\pi}{4}l^2(1-\epsilon^2)}} \frac{\exp(jkz)}{j\lambda z} \exp\left(j\frac{kr_0^2}{2z}\right) \Psi\{U(r_1)\} \Big|_{\rho=r_0/\lambda z}$$

The transmitted field distribution can be expressed as the difference of the field passing through an equal-diameter unobstructed aperture, and a hypothetical field of the same amplitude passing through an aperture equal to the obstruction. By the linearity of the Fourier-Bessel transform, $\Psi\{U(r_1)\} \pm \Psi\{V(r_1)\} = \Psi\{U(r_1) \pm V(r_1)\}$, we can write the received field as

$$\begin{aligned} U(r_0) &= \sqrt{\frac{P}{\frac{\pi}{4}l^2(1-\epsilon^2)}} \exp(jkz) \exp\left(j\frac{kr_0^2}{2z}\right) \left\{ \frac{kl^2}{j8z} \left[2 \frac{J_1(klr_0/2z)}{klr_0/2z} \right] - \frac{k\epsilon^2 l^2}{j8z} \left[2 \frac{J_1(k\epsilon l r_0/2z)}{k\epsilon l r_0/2z} \right] \right\} \\ &= \sqrt{\frac{P}{\frac{\pi}{4}l^2(1-\epsilon^2)}} \exp(jkz) \exp\left(j\frac{kr_0^2}{2z}\right) \frac{kl^2}{j4z} \left\{ \frac{J_1(klr_0/2z)}{klr_0/2z} - \epsilon^2 \frac{J_1(k\epsilon l r_0/2z)}{k\epsilon l r_0/2z} \right\} \end{aligned}$$

where

$$\Psi\left\{\text{circ}\left(\frac{r_1}{l/2}\right)\right\} = \left(\frac{l}{2}\right)^2 \frac{J_1(\pi l \rho)}{l \rho^2} \quad \Psi\left\{\text{circ}\left(\frac{r_1}{\epsilon l/2}\right)\right\} = \left(\frac{\epsilon l}{2}\right)^2 \frac{J_1(\pi \epsilon l \rho)}{\epsilon l \rho^2} \quad 0 \leq \epsilon \leq 1$$

are the Fourier-Bessel transforms of circular apertures with diameters equal to l and ϵl meters, respectively. The intensity distribution $I(r_0)$ in the receiver plane is the squared magnitude of the field distribution, hence

$$I(r_0) = |U(r_0)|^2 = \frac{P}{\frac{\pi}{4}l^2(1-\epsilon^2)} \left(\frac{kl^2}{4z} \right) \left(\frac{J_1(klr_0/2z)}{klr_0/2z} - \epsilon^2 \frac{J_1(k\epsilon lr_0/2z)}{k\epsilon lr_0/2z} \right)^2$$

$$I(0) = P \left(\frac{\frac{\pi}{4}l^2}{\lambda^2 z^2} \right) (1 - \epsilon^2)$$

Substituting $(r_0) = 0$ yields the on-axis intensity, which attains the maximum of the intensity distribution over the receiver plane, and assumes perfect alignment of the transmitter and receiver axes. Note that the on-axis intensity is inversely proportional to the square of the distance, but directly proportional to transmitter power P and transmitter area $\frac{\pi}{4}l^2$. In this form, the effect of the obstruction is to reduce the on-axis intensity by the area of the obstruction, $\frac{\pi}{4}\epsilon^2 l^2$. These equations can be used to estimate the optical power received by a ground-based aperture, both on-axis and with an arbitrary pointing error.

Next, we apply these results to compute the laser power, hence average number of photons per unit time, received by a ground-based aperture at a wavelength of $\lambda = 1.55 \times 10^{-6}$ m:

$$I(0) = P \left(\frac{\frac{\pi}{4}l^2}{\lambda^2 z^2} \right) (1 - \epsilon^2), \quad \epsilon = 0.2, \quad l = 0.5 \text{ m}, \quad z = 1.25(1.5 \times 10^{11})$$

$$= 1.875 \times 10^{11} \text{ m}, \quad P = 10 \text{ W},$$

$$I(0) = 10 \left(\frac{\frac{\pi}{4} \times 0.25}{(1.55 \times 10^{-6})^2 (1.875 \times 10^{11})^2} \right) (1 - 0.04)$$

$$= \frac{10 \frac{\pi}{16} (0.96)}{(2.9 \times 10^5)^2} = \frac{1.885}{8.4 \times 10^{10}} = 2.25 \times 10^{-11} \text{ W/m}^2$$

With $A_{rec} = 531 \text{ m}^2$, $P_{rec}(0) = 531 \times (2.25 \times 10^{-11}) = 1.192 \times 10^{-8} \text{ W}$.

At 1550 nm, the photon energy is $1.28 \times 10^{-19} \text{ J}$, therefore the average number of photons passing through the receiving aperture in 1 s is $(1.192 \times 10^{-8}) / (1.28 \times 10^{-19}) = 9.3 \times 10^{10}$ photons/s. This corresponds to 93 photons/ns.